

# Direct simulation of transition in an oscillatory boundary layer

By G. VITTORI<sup>1</sup> AND R. VERZICCO<sup>2</sup>

<sup>1</sup>Istituto di Idraulica Università di Genova, Via Montallegro 1, 16145 Genova, Italy

<sup>2</sup>Dipartimento di Meccanica e Aeronautica, Università di Roma 'La Sapienza',  
Via Eudossiana 18, 00184 Roma, Italy

(Received 18 July 1997 and in revised form 6 May 1998)

Numerical simulations of Navier–Stokes equations are performed to study the flow originated by an oscillating pressure gradient close to a wall characterized by small imperfections. The scenario of transition from the laminar to the turbulent regime is investigated and the results are interpreted in the light of existing analytical theories. The ‘disturbed-laminar’ and the ‘intermittently turbulent’ regimes detected experimentally are reproduced by the present simulations. Moreover it is found that imperfections of the wall are of fundamental importance in causing the growth of two-dimensional disturbances which in turn trigger turbulence in the Stokes boundary layer. Finally, in the intermittently turbulent regime, a description is given of the temporal development of turbulence characteristics.

---

## 1. Introduction

The boundary layer generated by the harmonic oscillations of a fluid parallel to an infinite fixed plate (Stokes layer) has received considerable attention. Besides being the prototype of unsteady boundary layers, the Stokes boundary layer is present in a variety of applications ranging from offshore and coastal engineering to biomedical sciences. The flow field in the laminar regime is well known (Stokes 1855). More recent investigations have addressed the problem of detecting transition to turbulence and of studying flow characteristics in the turbulent regime.

Turbulence has invariably been observed at Reynolds numbers larger than about 500, the resulting flow being characterized by the sudden, explosive appearance of turbulence bursts towards the end of the accelerating phases of the cycle (Hino, Sawamoto & Takasu 1976). Herein, the Reynolds number  $R_\delta$  is defined using the amplitude  $U_o^*$  of the velocity oscillations just outside the boundary layer and its conventional thickness  $\delta^*$  equal to  $(2\nu^*/\omega^*)^{1/2}$ , where  $\omega^*$  is the angular frequency of fluid oscillations and  $\nu^*$  the kinematic viscosity of the fluid. Experimental investigations show that turbulence is sustained throughout the decelerating phases, while during the early stages of the accelerating phases production of turbulence stops, the disturbances decay and the flow recovers its laminar behaviour. For increasing values of  $R_\delta$  turbulence affects larger parts of the cycle, till for  $R_\delta$  around 3500 (Jensen, Sumer & Fredøe 1989) turbulence is present throughout the whole cycle. It is worth pointing out that some experimental studies (see for example Hino *et al.* 1976) showed that for values of  $R_\delta$  smaller than 500 but larger than a value which is quite sensitive to the particular experimental set-up and ranges around 100, ‘small-amplitude’ pertur-

bations appear superimposed on the Stokes flow, even though the average velocity profiles exhibit only small deviations from the laminar case.

Therefore, on the basis of existing experimental observations, it can be concluded that four flow regimes can be identified: I the laminar regime; II a disturbed laminar regime, where 'small-amplitude' perturbations appear superimposed on the Stokes flow; III an intermittently turbulent flow, where bursts of turbulence appear explosively only during the decelerating phases of the cycle; IV a fully developed turbulent regime characterized by turbulence presence throughout the whole cycle.

Only recently have these experimental findings found an appropriate theoretical interpretation. It is generally agreed that transition is due to the local instability of the Stokes boundary layer and, therefore, much of the existing theoretical works have addressed the study of the time development of flow perturbations scaling with  $\delta^*$ . A first group of linear stability analyses proposed in the literature (Von Kerczeck & Davis 1974; Hall 1978) provided a description of the behaviour of disturbances averaged over a cycle, even though the time-periodic nature of the basic flow was explicitly considered. The analyses by Von Kerczek & Davis (1974) for the finite Stokes layer and by Hall (1978) for the infinite Stokes layer predicted the flow to be stable within the investigated range of the Reynolds number. A second group of stability analyses, based on a momentary criterion for instability (Von Kerczeck & Davis 1974; Tromans 1976; Blondeaux & Seminara 1979; Monkewitz 1983; Cowley 1987) were equally unsuccessful in explaining experimental findings. Indeed such analyses found that for  $R_\delta$  larger than 86 there are parts of the cycle near flow reversal during which the flow is unstable to initial perturbations of infinitesimal amplitude. However, even though the perturbations are characterized by a transient growth, they are found to experience a net decay over a cycle. Transition to turbulence has been recently shown to be related both to a receptivity mechanism and to nonlinear three-dimensional effects by the works by Blondeaux & Vittori (1994) and Wu (1992) respectively. Blondeaux & Vittori (1994) with a two-dimensional analysis showed that an aperiodic flow with many characteristics in common with the bursting turbulent flow detected experimentally can be generated by the interaction among the momentarily unstable modes studied by Blondeaux & Seminara (1979) and the forced modes induced by infinitesimal wall imperfections. Another possible mechanism for the generation of a bursting flow in a flat Stokes layer was pointed out by Wu (1992) who considered the nonlinear evolution of a high-frequency inviscid disturbance composed of a two-dimensional wave and a pair of oblique waves. He showed that the amplitudes of the three waves can develop a finite-time singularity, the explosive growth being induced by the nonlinear interaction inside critical layers. Later Wu, Lee & Cowley (1995) also considered viscous effects which, for large values of the Reynolds number, were found to become important first in the critical layers far from the wall and then in the wall layer.

On the numerical side, by means of direct simulations of Navier–Stokes equations, Spalart & Baldwin (1987) and Akhavan, Kamm & Shapiro (1991 *b*) found, in accordance with linear stability theories, that initial disturbances of small amplitude always experience a net decay. On the other hand they found in accordance with Wu (1992)'s analysis that two-dimensional disturbances of large amplitude when interacting with three-dimensional perturbations can trigger transition to turbulence. However neither Spalart & Baldwin (1987) nor Akhavan *et al.* (1991 *b*) explained how a large-amplitude two-dimensional wave can be generated within the boundary layer in the first place. More recently, a preliminary numerical investigation by Verzicco & Vittori (1996) has shown that wall imperfections are of fundamental importance in triggering transition to turbulence in the Stokes layer.

In the present contribution the flow induced by an oscillatory pressure gradient close to a flat wall but characterized by small imperfections is studied by means of a three-dimensional numerical simulation of Navier–Stokes and continuity equations. By starting from the achievements of Verzicco & Vittori (1996), the mechanism of transition from the laminar regime to the ‘disturbed laminar’ one and from the latter to the intermittently turbulent regime is investigated. Moreover, the characteristics of the flow field in the different regimes are presented. The work of Blondeaux & Vittori (1994) is extended by taking into account three-dimensional effects which, as Akhavan *et al.* (1991 *b*) Wu (1992) and Wu *et al.* (1993) showed, play an important role in secondary instability. Moreover, nonlinear effects in the evolution of flow disturbances, neglected by Akhavan *et al.* (1991 *b*), are included and are shown to influence the characteristics of the flow field even for values of Reynolds number close to the critical conditions.

From a mathematical point of view it cannot be stated that the wall imperfections we consider are of infinitesimal amplitude since our analysis is not based on a perturbation approach but on the numerical simulation of the full Navier–Stokes equations. However, the results described in §3 and obtained for amplitudes  $\epsilon^*$  of the wall waviness which are quite small compared with  $\delta^*$  (values of  $\epsilon^*/\delta^*$  of order  $10^{-3}$ ,  $10^{-4}$  and  $10^{-5}$  are considered) show that transition to turbulence can be triggered without resorting to the introduction of initial perturbations of the flow field which are of significant amplitude when compared with the basic Stokes flow.

The structure of the rest of the paper is the following. In the next section we formulate the problem and describe briefly the numerical method. The third section is devoted to detecting transition from the laminar to the turbulent regime. In the fourth section, the structure of the flow field in the disturbed laminar and intermittently turbulent regimes is investigated. The last section is devoted to the conclusions.

## 2. The problem

In the present work we study the boundary layer generated, close to a wall, by an oscillating pressure gradient described by

$$\frac{\partial P^*}{\partial x_1^*} = -\rho^* U_o^* \omega^* \sin(\omega^* t^*), \quad \frac{\partial P^*}{\partial x_2^*} = 0, \quad \frac{\partial P^*}{\partial x_3^*} = 0, \quad (1)$$

where  $x_1^*$ ,  $x_2^*$  and  $x_3^*$  indicate streamwise, cross-stream and spanwise coordinates respectively (see figure 1). The wall is not perfectly flat but characterized by a small waviness and its profile  $\eta^*$  is given by the superimposition of sinusoidal components

$$x_2^* = \epsilon^* \eta(x_1^*, x_3^*) = \epsilon^* \sum_{n=1}^N a_n \cos(\alpha_n^* x_1^* + \gamma_n^* x_3^* + \phi_n), \quad (2)$$

where  $\epsilon^* a_n$  denotes the amplitude of the  $n$ th component which is characterized by wavenumbers  $\alpha_n^*$  and  $\gamma_n^*$  in the  $x_1^*$ - and  $x_3^*$ -directions respectively and by a random phase  $\phi_n$ . In (1)  $\rho^*$  is the constant density of the fluid,  $U_o^*$  and  $\omega^*$  are the amplitude and the angular frequency of fluid velocity oscillations induced by (1) far from the wall. A star is used to denote dimensional quantities and use is made of dimensionless variables defined as

$$\left. \begin{aligned} t &= t^* \omega^*, & \mathbf{x} &= (x_1, x_2, x_3) = \frac{(x_1^*, x_2^*, x_3^*)}{\delta^*}, \\ \mathbf{u} &= (u_1, u_2, u_3) = \frac{(u_1^*, u_2^*, u_3^*)}{U_o^*}, & p &= \frac{p^*}{\rho^* (U_o^*)^2}. \end{aligned} \right\} \quad (3)$$

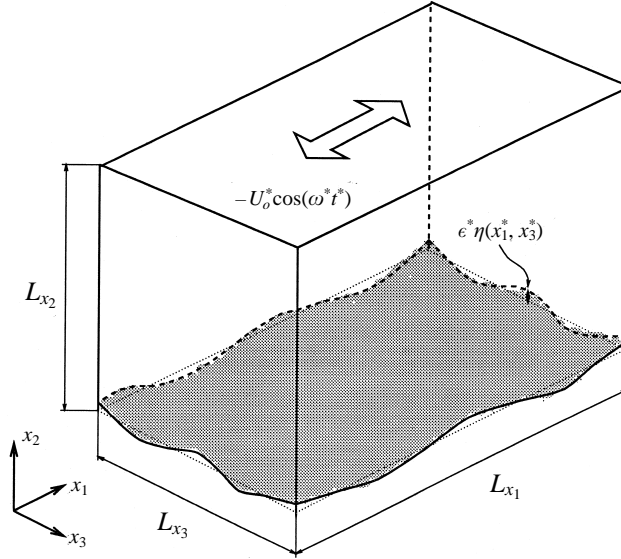


FIGURE 1. Sketch of the problem.

In (3)  $t^*$  is time,  $u_1^*, u_2^*, u_3^*$  the fluid velocity components along  $x_1^*, x_2^*$  and  $x_3^*$  respectively and  $\delta^*$  is the conventional thickness of the viscous boundary layer close to the wall defined as  $(2\nu^*/\omega^*)^{1/2}$ ,  $\nu^*$  being the kinematic viscosity of the fluid.

The problem is thus posed by Navier–Stokes and continuity equations:

$$\frac{\partial \mathbf{u}}{\partial t} + \frac{R_\delta}{2} \nabla \cdot (\mathbf{u}\mathbf{u}) = -\frac{R_\delta}{2} \nabla p + \mathbf{i}_{x_1} \sin(t) + \frac{1}{2} \nabla^2 \mathbf{u} \quad (4a)$$

$$\nabla \cdot \mathbf{u} = 0 \quad (4b)$$

where  $\mathbf{i}_{x_1}$  is the unit vector in the streamwise direction. The governing equations are solved numerically in a computational domain of dimensions  $L_{x_1}, L_{x_2}$  and  $L_{x_3}$  in the streamwise, cross-stream and spanwise directions respectively.

At the lower wall the no-slip condition is enforced:

$$(u_1, u_2, u_3) = 0 \quad \text{at} \quad x_2 = \epsilon \eta(x_1, x_3). \quad (5)$$

Having assumed the amplitude of the wall waviness to be much smaller than the thickness of the laminar boundary layer ( $\epsilon = \epsilon^*/\delta^* \ll 1$ ), boundary condition (5) can be approximated as

$$(u_1, u_2, u_3) = -\epsilon \eta(x_1, x_3) \frac{\partial}{\partial x_2} (u_1, u_2, u_3) + O(\epsilon^2) \quad \text{at} \quad x_2 = 0. \quad (6)$$

Note that (6) is an approximation of the boundary condition (5) within the accuracy of the numerical method itself. Indeed the numerical scheme adopted is second order accurate in space and in all the simulations  $\epsilon$  has been taken to be smaller than the first computational step in the  $x_2$ -direction.

At  $x_2 = L_{x_2}$  a symmetry condition is imposed:

$$\frac{\partial}{\partial x_2} (u_1, u_3) = 0, \quad u_2 = 0, \quad (7)$$

which is equivalent to requiring the vanishing of tangential stresses far from the wall and to imposing that the flow field far from the wall tends to  $(-U_o^* \cos \omega^* t, 0, 0)$ .

Finally, the turbulent flow is assumed to be homogeneous in the streamwise and spanwise directions and periodic boundary conditions are thus enforced along the  $x_1$ - and  $x_3$ -axes. The use of periodic boundary conditions in the homogeneous directions is justified if the computational box (period) is large enough to include the largest eddies in the flow. Checks on the size of the computational box, reported in the following, have been carried out to verify this assumption.

The computational mesh is uniform in the streamwise and spanwise directions while in the cross-stream one a non-uniform mesh has been used to cluster the gridpoints in the vicinity of the wall where gradients are expected to be stronger. The clustering function is

$$x_2 = L_{x_2} \left( 1 + \frac{\tanh[a(\xi - 1)]}{\tanh(a)} \right), \quad (8)$$

where  $0 \leq \xi \leq 1$  is the computational domain where equispaced grid points are introduced and  $a$  is an appropriate stretching parameter.

The numerical method solves the problem in primitive variables using standard centred second-order finite difference approximations of the spatial derivatives, while the time-advancement of Navier–Stokes equations employs a fractional-step method extensively described by Kim & Moin (1985), Orlandi (1989) and Rai & Moin (1991). The non-solenoidal intermediate velocity field is evaluated by means of a third-order Runge–Kutta scheme to discretize convective terms together with a Crank–Nicolson scheme the diffusive terms. The implicit treatment of the viscous terms would require for the inversion of large sparse matrices which are reduced to three tridiagonal matrices by a factorization procedure with an error of order  $(\Delta t)^3$  (Beam & Warming 1976). Then, by forcing the continuity equation (4b) a Poisson equation for the pressure field is obtained which is readily solved by taking advantage of the imposed periodicity in the  $x_1$ - and  $x_3$ -directions. More details on the numerical approach can be found in Kim & Moin (1985) and Rai & Moin (1991).

In order to check the numerical code, preliminary computations have been performed to compare the results with previous analytical solutions which hold for small or moderate values of the Reynolds number  $R_\delta$  (Blondeaux 1990; Vittori 1992). Figure 2 shows an example of the comparison between the numerical solution and the analytical one obtained by Blondeaux (1990) assuming small values of  $\epsilon$  and by considering a two-dimensional wall wavyness. It appears that the numerical solution is practically indistinguishable from the theoretical one. A good agreement has also been found when comparing the outputs of the numerical code with the results described in Vittori (1992) which hold for moderate values of  $R_\delta$ , small values of  $\epsilon$  and a three-dimensional wall wavyness. Then the numerical code has been run for different values of the Reynolds number  $R_\delta$  ranging from 50 to 1200. Some parameters of the wall profile (2) have been kept fixed in all the runs. In particular a wall profile with two harmonic components ( $N = 2$ ) has been used. The first component is two-dimensional and has wavenumber characteristic of the most unstable two-dimensional disturbance detected by Blondeaux & Seminara (1979), i.e.  $\alpha_1 = 0.5$  and  $\gamma_1 = 0$ . The second component has been chosen with the same spanwise spatial periodicity as that of the three-dimensional perturbations which Akhavan *et al.* (1991 *b*) showed to have the maximum growth rate when interacting with a pre-existing finite amplitude two-dimensional wave ( $\gamma_2 = 1, \alpha_2 = 0$ ). Moreover,  $a_1 = 1, a_2 = 0.1$  and  $\phi_1 = \phi_2 = 0$ . If not otherwise specified  $\epsilon$  has been set equal to 0.005 which is a value typical of the order

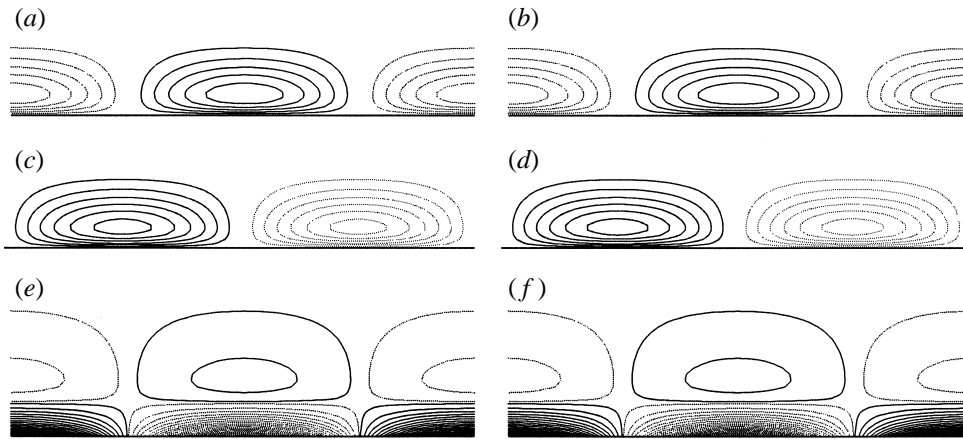


FIGURE 2. Contour plot of the vertical velocity component for  $R_\delta = 50$ ,  $\epsilon = 0.005$ ,  $N = 1$ ,  $a_1 = 1$ ,  $\alpha_1 = 0.5$ ,  $\gamma_1 = 0$ : (a, c, e) numerical results, (b, d, f) analytical solution: (a, b)  $t = 0$ , (c, d)  $t = \pi/4$ , (e, f)  $t = \pi/2$  ( $\Delta v_2 = \pm 1.1 \times 10^{-4}$ ) —, positive; - - - -, negative values.

of magnitude of imperfections for a mirror-shine smooth wall. However, in order to investigate the effect of the amplitude of the wall wavyness in the transition process, other values of  $\epsilon$  have been considered and in particular  $\epsilon = 0.0005$  and  $\epsilon = 0.00005$ . The size of the computational domain has been fixed for all the runs as  $25.13\delta^*$ ,  $12.57\delta^*$  and  $25.13\delta^*$  in the  $x_1^*$ ,  $x_3^*$  and  $x_2^*$  directions respectively and the number of grid points in these directions is 65, 33 and 65 respectively. The stretching parameter  $a$  in equation (8) has been set equal to 1.8 so that 11 grid points were clustered in the direction normal to the wall in the first unit length. From the results shown in the following (see for example figures 5, 8, 9 and 10) it can be appreciated that the value chosen for  $a$  is appropriate for describing the vortex structures appearing in the nearwall region for the range of Reynolds numbers investigated here.

Checks have been performed on the numerical grid and on the box dimensions. First, the run for  $R_\delta = 800$ , during which turbulence is observed, has been repeated with the same box dimensions but with a larger number of grid points (97, 97 and 49 in the streamwise, cross-stream and spanwise directions respectively). All the averaged quantities describing turbulence have shown no significant change. For example the time average of the vertically integrated kinetic energy of turbulence defined in the following (equation (13)) takes the value  $1.15 \times 10^{-2}$  for the reference simulation (average over 13 periods) and the value  $1.13 \times 10^{-2}$  (average over four periods) for the finer grid simulation and the difference is thus less than 2%. Then the simulation has been repeated for a larger box. In particular the box dimensions in the  $x_1$ - and  $x_3$ -directions have been doubled together with the number of grid points. In this case too, no significant change in turbulence characteristics has been detected even though the differences with respect to the reference simulation increase. For example the vertically integrated kinetic energy of turbulence turns out to be  $1.24 \times 10^{-2}$  (average over four periods).

To shorten the length of the transient, the runs have been started from the flow fields determined analytically in Vittori (1992) which differ from the Stokes solution for quantities of order  $\epsilon$ . However, the flow field regime does not depend on the initial conditions. The attainment of regime conditions was judged on the basis of the temporal development of the velocity components at a fixed position and of the vertically

---

Run number	$R_\delta$	Length of the simulation	Transient time discarded in the treatment of the results
1	100	$6\pi$	$2\pi$
2	200	$6\pi$	$2\pi$
3	400	$10\pi$	$4\pi$
4	500	$10\pi$	$4\pi$
5	550	$26\pi$	$20\pi$
6	600	$32\pi$	$20\pi$
7	800	$30\pi$	$4\pi$
8	1000	$16\pi$	$4\pi$
9	1200	$16\pi$	$4\pi$

---

TABLE 1.

integrated specific turbulent kinetic energy. Even though in most cases convergence was obtained at the end of the first cycle, the first two cycles were discarded. However, in the vicinity of transitional Reynolds numbers, the attainment of a statistical steady state was somewhat slower and as many as 10 cycles were required to reach regime conditions. In such cases a longer transient was discarded. In table 1 the length of the numerical simulation is reported for each run together with the number of initial periods discarded to determine averaged quantities characterizing turbulence.

### 3. Transition to turbulence

The flow fields obtained by means of the present numerical code show the same features as observed in previous experimental studies (Hino *et al.* 1976; Jensen *et al.* 1989; Akhavan, Kamm & Shapiro 1991 *a*; Eckmann & Grotberg 1991). In particular for Reynolds numbers up to 100, the flow is the same as that obtained analytically by Vittori (1992) and differs from the Stokes solution only for quantities of order  $\epsilon$ , induced by the presence of the waviness of the wall. Therefore, this flow regime can be defined as laminar. For values of the Reynolds number in the range 100–550 significant two-dimensional disturbances are observed, the amplitude of which, starting from small values, grows during parts of the cycle and reaches values much larger than  $\epsilon$ , and then decreases in the remaining parts and becomes small again. From figure 3(b), where the time development of the cross-stream component of velocity at a fixed position is shown for  $R_\delta = 500$ , it can be immediately observed that disturbances of the flow start to grow at the end of the decelerating part of the cycle, reach their maximum intensity at the beginning of the accelerating part and then slowly decay (notice that the external flow progresses as  $-U_o^* \cos \omega^* t^*$ ). However, note that in this flow regime the disturbances are periodic (see figure 3b) and two-dimensional (see figure 3c). Hence the flow is deterministic and the regime cannot be called turbulent but, according to the existing literature, the term ‘disturbed laminar’ will be used. Characteristics of the disturbed-laminar regime can be detected by considering the Fourier components in the  $x_1$ - and  $x_3$ -directions of the vertically integrated kinetic energy ( $E$ ) of the perturbations, which are computed after having decomposed the flow field into an averaged and in a fluctuating part. Because of the supposed quasi-homogeneity of the flow in the streamwise and spanwise directions, to obtain averaged quantities denoted by  $\langle \cdot \rangle$ , first spatial averages in the  $x_1$ - and  $x_3$ -directions have been performed and then because of the time-periodic nature of

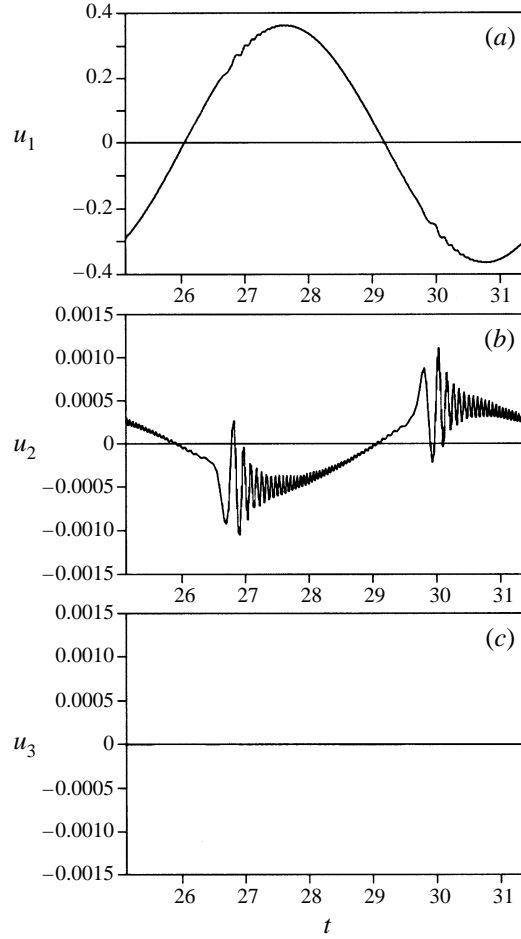


FIGURE 3. Temporal development of streamwise (a), cross-stream (b) and spanwise (c) velocity components at  $x_1 = 3.93$ ,  $x_2 = 0.25$ ,  $x_3 = 3.93$  for  $\epsilon = 0.005$ ,  $R_\delta = 500$ .

the the flow, the average over flow fields with a phase lag of  $2\pi$  has been computed:

$$\langle f(x_2, t) \rangle = \frac{1}{N_P} \sum_{n=1}^{N_P} \left\{ \frac{1}{L_{x_1} L_{x_3}} \int_0^{L_{x_1}} \int_0^{L_{x_3}} f(x_1, x_2, x_3, t + 2\pi n) dx_1 dx_3 \right\}. \quad (9)$$

In (9)  $N_P$  indicates the number of simulated periods.

If  $u'_1, u'_2$  and  $u'_3$  denote the fluctuating parts of the three velocity components

$$(u_1, u_2, u_3) = (\langle u_1 \rangle, \langle u_2 \rangle, \langle u_3 \rangle) + (u'_1, u'_2, u'_3), \quad (10)$$

the vertically integrated kinetic energy of flow disturbances and its Fourier components are defined by

$$E(x_1, x_3, t) = \int_0^{L_{x_2}} \frac{1}{2} (u_1'^2 + u_2'^2 + u_3'^2) dx_2, \quad (11)$$

$$E(x_1, x_3, t) = \sum_{m=-N_{x_3}}^{N_{x_3}} \sum_{n=-N_{x_1}}^{N_{x_1}} \hat{E}_{nm}(t) e^{\frac{im2\pi x_1}{L_{x_1}}} e^{im \frac{2\pi x_3}{L_{x_3}}}, \quad (12)$$



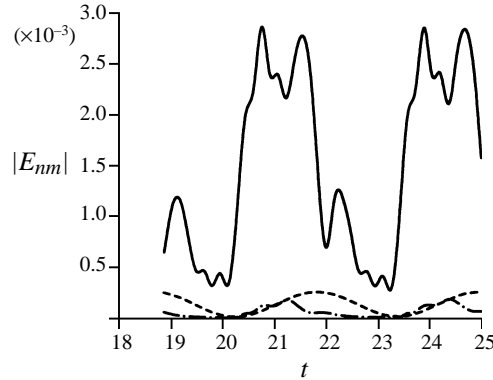


FIGURE 4.  $|\hat{E}_{nm}|$  as a function of time ( $\epsilon = 0.005$ ,  $R_\delta = 500$ ). —,  $n = 2$ ,  $m = 0$ ; - - -,  $n = 0$ ,  $m = 2$ ; - · - · - ·,  $n = 4$ ,  $m = 0$ .

where  $2N_{x_1} + 1$  and  $2N_{x_3} + 1$  are the number of grid points in the  $x_1$ - and  $x_3$ -directions respectively. Since  $E(x_1, x_3, t)$  is a real-valued quantity, it can be easily shown that

$$|\hat{E}_{nm}| = |\hat{E}_{n-m}| = |\hat{E}_{-nm}| = |\hat{E}_{-n-m}|$$

(the symbol  $||$  denotes the modulus of a complex quantity). Because at present we are interested in investigating the temporal evolution of the modulus of the different components of kinetic energy, only the values of  $|\hat{E}_{nm}|$  for  $0 \leq n \leq N_{x_1}$  and  $0 \leq m \leq N_{x_3}$  will be presented.

The results obtained have shown that in the disturbed laminar regime, the kinetic energy of the flow perturbations is significant only for spatial components characterized by wavenumbers in the streamwise and spanwise directions equal to those of the wall waviness. Moreover, the component forced by the two-dimensional disturbance of the wall is found to have the largest value throughout the cycle. As an example, the temporal development of the significant components of  $|E_{nm}|$  is shown in figure 4 for  $R_\delta = 500$ . It can be observed that  $|\hat{E}_{20}|$  grows in the very last part of the decelerating phase and in the early stages of the accelerating phase. Moreover, nonlinear effects drive a small growth of  $|\hat{E}_{40}|$  too. During the initial growth of the disturbances only two-dimensional components of the flow are triggered. On the other hand as flow accelerates, a weak growth of the three-dimensional component ( $|\hat{E}_{02}|$ ) can be seen followed by a rapid decay of all the components at the end of the accelerating part of the cycle.

In order to get more insight into the structure of the flow field, the time development of vorticity  $\Omega$  has been considered. In figure 5 the spanwise component  $\Omega_3$  is plotted in a vertical plane parallel to the flow direction at different instants within the cycle. To show more clearly the features of vortex structures, the part of  $\Omega_3$  related to Stokes flow and independent of  $x_1$  has been removed beforehand. The results shown in figure 5 along with the observation that the other components of vorticity ( $\Omega_1$  and  $\Omega_2$ ) are three orders of magnitude smaller than  $\Omega_3$  indicate that the growth of the perturbations leads to the formation of two-dimensional coherent structures characterized by an axis parallel to the spanwise direction. At the very end of the decelerating phase (see figure 5a) and at the beginning of the accelerating one, clockwise and counterclockwise  $\Omega_3$  vorticity originated near the wall tends to coalesce and to form patches located in the near-wall region, which recur in the streamwise direction at a distance equal to approximately  $12 \delta^*$ . As the external flow accelerates, vorticity is convected in the streamwise direction originating elongated

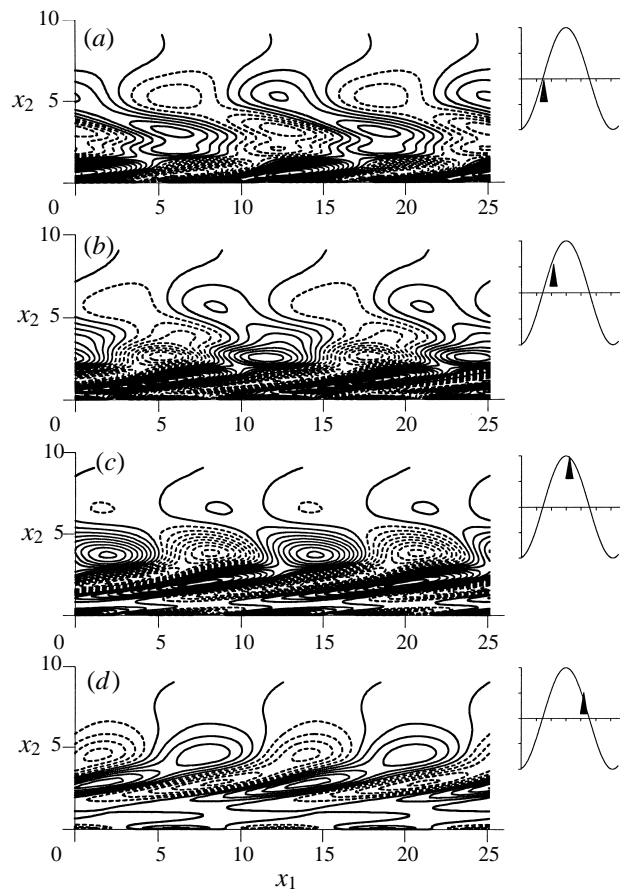


FIGURE 5. Instantaneous snapshots of the spanwise component of vorticity ( $\Omega_3$ ) in the plane  $x_3 = 5.9$  (contour lines with  $\Delta\Omega_3 = 2 \times 10^{-3}$ ) for  $\epsilon = 0.005$ ,  $R_\delta = 500$ . —, positive vorticity; - - -, negative vorticity. (a)  $t = 20.4$ ; (b)  $t = 21.0$ ; (c)  $t = 22.0$ ; (d)  $t = 22.9$ .

vortex structures (see figure 5*b* where the external flow is from left to right) the tip of which moves far from the wall because of self-induced velocity. When the external flow reaches its maximum intensity (figure 5*c*), the vortex structures are folded back and then, as the flow decelerates (figure 5*d*), viscous diffusion causes a decrease of vorticity intensity both close to the wall and far from it. In the following half period, the process repeats similarly.

The results shown in figure 5 along with those obtained for  $R_\delta$  falling in the range (100, 550) indicate that in the disturbed laminar regime the disturbances which appear are periodic in the streamwise direction with a wavenumber equal to that forced by the wall waviness. Moreover, flow disturbances grow at flow reversal and decay during the decelerating phases of the cycle. Finally, although three-dimensional perturbations are forced by wall waviness along with the two-dimensional ones, they do not grow and keep quite small. Hence the results obtained suggest that the momentary instability mechanism investigated by Blondeaux & Seminara (1979) is effective every half a cycle and gives rise to perturbations of the Stokes solution but it is unable to trigger turbulence. The results obtained so far have shown fluctuations in the flow field periodic both in time and in the streamwise direction produced

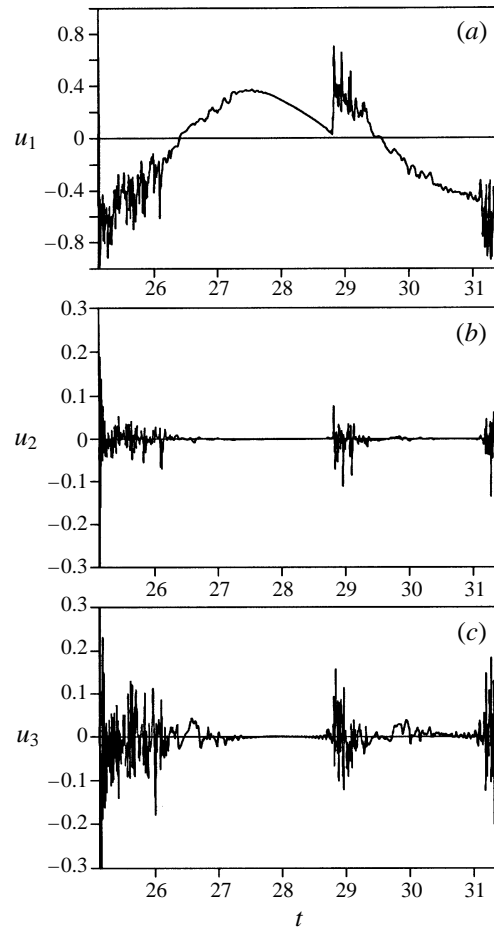


FIGURE 6. Temporal development of streamwise (a), cross-stream (b) and spanwise (c) velocity components at  $x_1 = 3.93$ ,  $x_2 = 0.25$ ,  $x_3 = 3.93$  for  $\epsilon = 0.005$ ,  $R_\delta = 1000$ .

by the appearance of vortices, the main axis of which is parallel to the spanwise direction. No evidence has been found of the low-speed streaks or of the other coherent vortex structures detected experimentally by Sarpkaya (1993) for  $R_\delta$  in the range 420–520. It is worthwhile to mention that Sarpkaya's experiments were conducted by visualizing the flow on the surface of a long cylindrical body immersed in a sinusoidally oscillating flow. Even if the Stokes parameter, defined by Sarpkaya (1993) as the ratio between the radius of the cross section of the cylinder and the boundary layer thickness, was kept large in order that the mean flow be independent of it, the present results seem to indicate that the Stokes parameter could influence the stability of the flow. In fact structures similar to those detected by Sarpkaya (1993) appear in the present geometry when  $R_\delta$  falls in the intermittently turbulent regime, i.e. for slightly larger Reynolds numbers.

As Reynolds number exceeds 550, a different flow regime is observed which, following experimentalists, we will call the intermittently turbulent regime. From figure 6 where the three velocity components at a fixed position are shown for  $R_\delta = 600$ , it can be appreciated that the velocity components show intense three-dimensional random fluctuations. In this flow regime perturbations of the Stokes

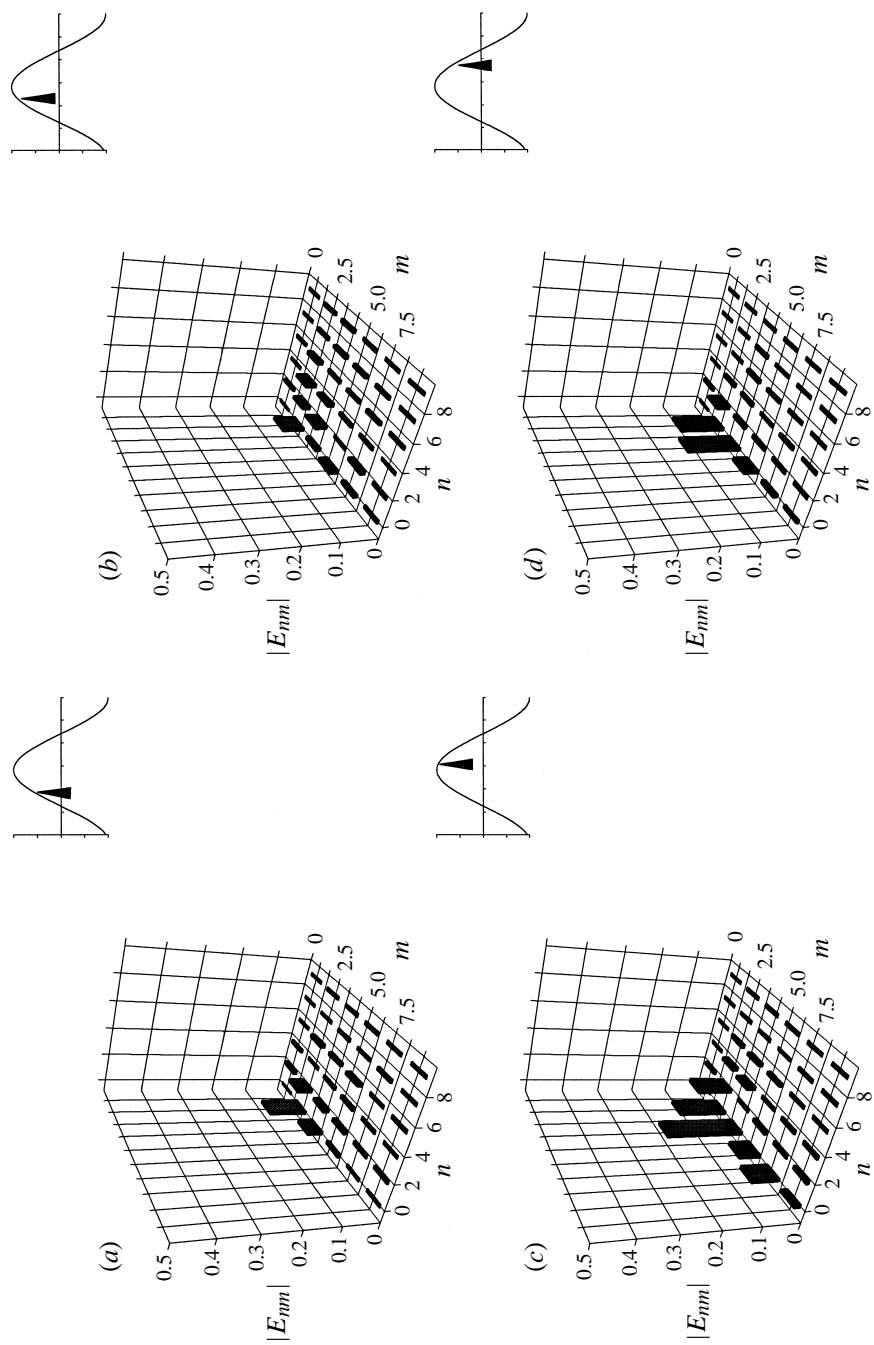


FIGURE 7.  $|\hat{E}_{nm}|$  defined by (12) at different instants in the cycle ( $\epsilon = 0.005$ ,  $R_3 = 600$ ). (a)  $t = 83.9$ ; (b)  $t = 84.2$ ; (c)  $t = 85.1$ ; (d)  $t = 85.8$ .

flow start to appear towards the end of the accelerating phases of the cycle and are sustained during part of the decelerating phases. As  $R_\delta$  is increased, the turbulent velocity fluctuations increase in strength and the decelerating part of the cycle during which they are observed becomes longer.

From figure 7, where the components  $|\hat{E}_{nm}|$  defined by (12) are shown at different instants in the cycle for  $R_\delta = 600$ , it can be observed that the fluctuating part of the flow is now strongly three-dimensional, since the number of non-vanishing harmonics in the spanwise direction becomes even larger than the corresponding number in the streamwise direction. The present results support Akhavan *et al.*'s (1991 *b*) indications that the most unstable three-dimensional mode is characterized by a wavenumber equal to 1.0 in the spanwise direction, since the amplitude of the corresponding Fourier component ( $|\hat{E}_{02}|$ ) shows an order of magnitude comparable to that of the two-dimensional components and reaches its maximum intensity at the end of the accelerating phase. However, the present results indicate that the width of the spectrum of the unstable modes is very large even for  $R_\delta$  equal to 600. Therefore, as the Reynolds number exceeds the critical value of 550, three-dimensional effects appear to be essential in the dynamics of the flow field. Considering the temporal evolution of the components  $|\hat{E}_{nm}|$ , it can be seen that disturbances start to grow during the accelerating part of the cycle but reach their maximum intensity at the beginning the decelerating part of the cycle. At the end of the decelerating phase, the disturbances rapidly decay and attain low levels of energy. Again this finding agrees with the experimental results of Akhavan *et al.* (1991 *a*) (see figure 10 of their paper). The vorticity field shows some similarities with the 'disturbed laminar regime': vorticity patches form at the beginning of the accelerating phases, are then stretched in the streamwise direction and folded back when the external flow velocity is maximum. Notwithstanding these similarities, both quantitative and qualitative differences are present. In fact in the intermittently turbulent regime,  $\Omega_1$  and  $\Omega_2$  have the same order of magnitude as  $\Omega_3$ , indicating that three dimensional effects are no longer negligible but play a significant role. Moreover, from figure 8, which shows  $\Omega_3$  in a plane parallel to the  $(x_1, x_2)$ -axes for  $R_\delta = 600$ , it can be seen that vortex structures are generated at the beginning of the accelerating part of the cycle then they grow in the late accelerating and early decelerating phases. As the external flow further decelerates, the coherent vortices break and originate much smaller vortex structures which then decay because of viscous effects. Inspection of figure 9, where  $\Omega_3$  is plotted in a plane parallel to the wall for the same times as figure 8 shows more clearly the generation of elongated streaks parallel to the streamwise direction which reach their maximum intensity for  $t = 82$  (see figure 9 *c*) and then for  $t = 82.6$  break, covering all the plane with small-scale vortices (figure 9 *d*) which subsequently dissipate because of viscous effects. Figure 10 shows that the coherent structures created during flow acceleration rotate preferentially around an axis parallel to the  $x_3$ -direction and the highest values of  $\Omega_1$  are found during the decelerating phases of the cycle when small-scale vortices are present. Finally, in the intermittently turbulent regime the dynamics of the vortex structures is not periodic.

When larger values of the Reynolds number are considered, flows similar to that detected for  $R_\delta$  equal to 600 are observed even though, due to stronger nonlinear effects, the energy appears to be spread among more modes and smaller structures appear in the temporal development of vorticity.

Further investigations have been carried out to better understand the role of the wall in triggering and maintaining turbulence. First, both in the disturbed laminar and in the intermittently turbulent regime the runs have been continued, after the

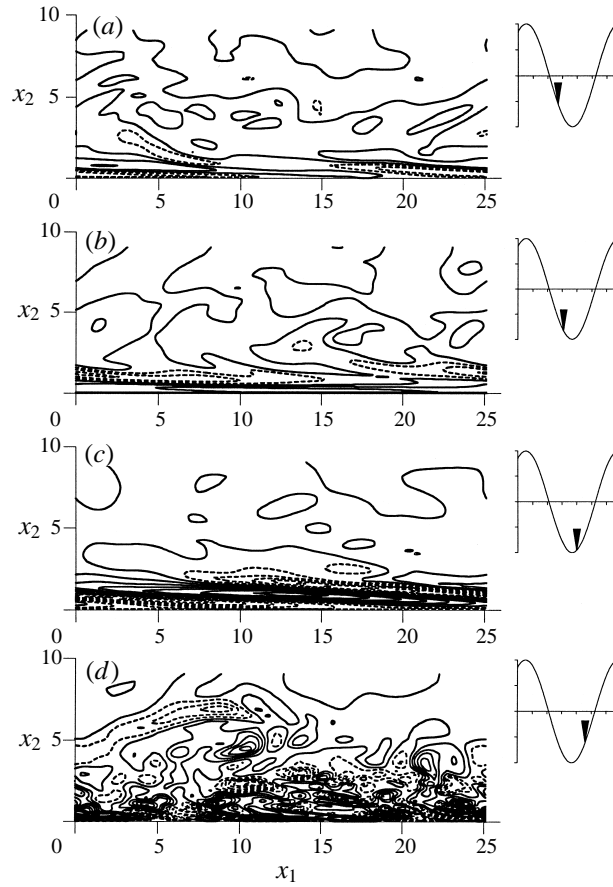


FIGURE 8. Instantaneous snapshots of the spanwise component of vorticity ( $\Omega_3$ ) in the plane  $x_3 = 3.93$  (contour lines with  $\Delta\Omega_3 = 0.05$ ) for  $\epsilon = 0.005$ ,  $R_\delta = 600$ ; —, positive vorticity; - - -, negative vorticity. (a)  $t = 80.7$ ; (b)  $t = 81.1$ ; (c)  $t = 82.0$ ; (d)  $t = 82.6$ .

transient was completed, removing the waviness of the wall. It is found that in the disturbed laminar regime the flow recovers a laminar behaviour in accordance with linear stability analyses (Von Kerczek & Davis 1974; Hall 1978) and previous numerical investigations (Spalart & Baldwin 1987; Akhavan *et al.* 1991 *b*). In the intermittently turbulent regime, after a short transient, turbulent fluctuations persist and the level of turbulent kinetic energy remains unaffected.

In order to investigate the effect of the amplitude of the imperfections of the wall in triggering turbulence, two new series of runs were performed with amplitudes one and two orders of magnitude smaller. The results are shown in figure 11 where the time-averaged, vertically integrated specific kinetic energy  $\bar{E}$  of the perturbations is plotted versus  $R_\delta$ . The value of  $\bar{E}$  is defined by

$$\bar{E} = \frac{1}{2\pi} \int_{t_0}^{t_0+2\pi} dt \left[ \frac{1}{A} \int_V \frac{1}{2}(u_1^2 + u_2^2 + u_3^2) dV \right], \quad (13)$$

where  $V$  indicates the volume of the computational box and  $A$  its area against the plate. In figure 11 the three flow regimes previously defined can be clearly identified.

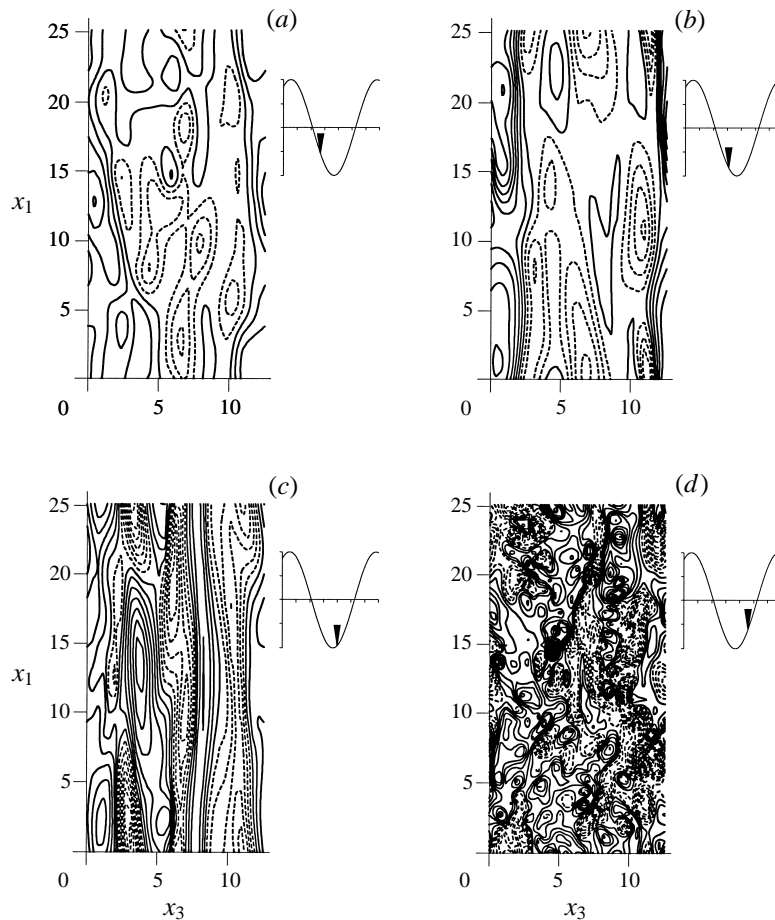


FIGURE 9. Instantaneous snapshots of the spanwise component of vorticity ( $\Omega_3$ ) in the plane  $x_2 = 0.89$  (isolines with step  $\Delta = 0.05$ ) for  $\epsilon = 0.005$ ,  $R_\delta = 600$ ; —, positive vorticity; - - -, negative vorticity. (a)  $t = 80.7$ ; (b)  $t = 81.1$ ; (c)  $t = 82.0$ ; (d)  $t = 82.6$ .

In the laminar regime ( $R_\delta$  less than a value  $R_{\delta 1}$  ranging around 100)  $\bar{E}$  is practically independent of  $R_\delta$  and is proportional to  $\epsilon^2$  in accordance with Blondeaux (1990) and Vittori (1992). In the disturbed laminar regime ( $R_{\delta 1} < R_\delta < R_{\delta 2}$ , where  $R_{\delta 2}$  depends on  $\epsilon$ )  $\bar{E}$  strongly depends both on  $R_\delta$  and on  $\epsilon$ . Finally, in the intermittently turbulent regime ( $R_\delta > R_{\delta 2}$ )  $\bar{E}$  is weakly dependent on  $R_\delta$  and is independent of  $\epsilon^2$ . Moreover, from figure 11 it can be appreciated that  $R_{\delta 1}$ ,  $R_{\delta 2}$  and  $\bar{E}$  in the laminar and disturbed laminar regimes are all affected by the value of  $\epsilon$ . It is thus explained why the appearance of disturbances is so sensitive to the characteristics of the experimental apparatus. For example, perturbations of the Stokes flow for  $R_\delta$  in the range (100, 500) have been detected by Hino *et al.* (1976) while Jensen *et al.* (1989) were unable to observe them.

It is worth mentioning that the flow regime observed experimentally by Jensen *et al.* (1989), where intense turbulent fluctuations are present throughout the whole cycle (fully developed turbulent regime), is not reproduced in the present simulations because the high computational costs do not allow the direct simulation of Navier–Stokes equation for  $R_\delta$  as large as 3500.

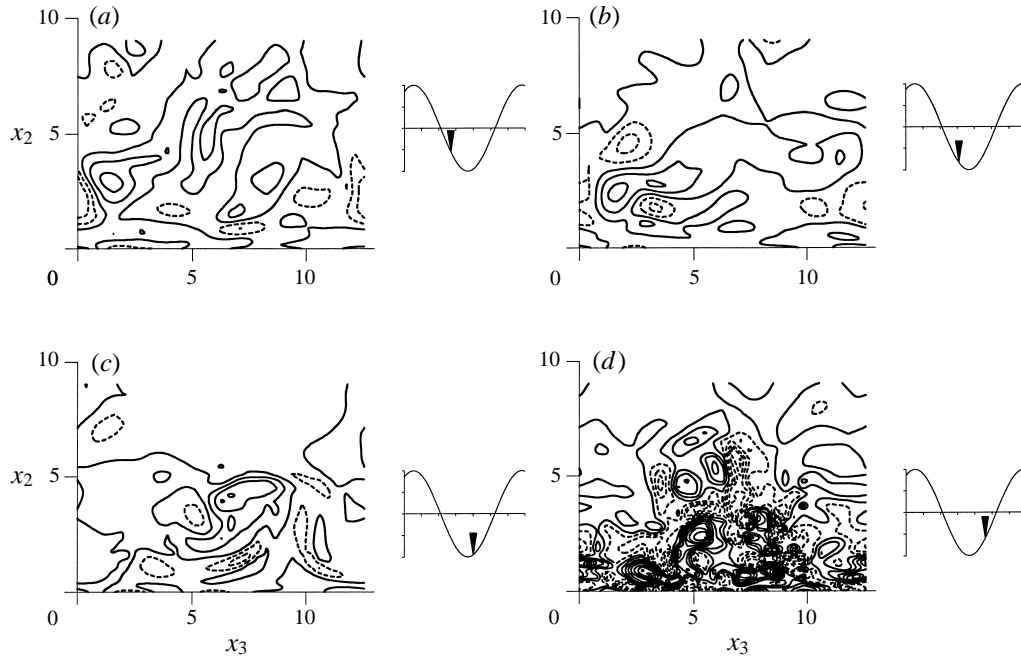


FIGURE 10. Instantaneous snapshots of the streamwise component of vorticity ( $\Omega_1$ ) in the plane  $x_1 = 12.57$  (contour lines with  $\Delta\Omega_1 = 0.05$ ) for  $\epsilon = 0.005$ ,  $R_\delta = 600$ ; —, positive vorticity; - - -, negative vorticity. (a)  $t = 80.7$ ; (b)  $t = 81.1$ ; (c)  $t = 82.0$ ; (d)  $t = 82.6$ .

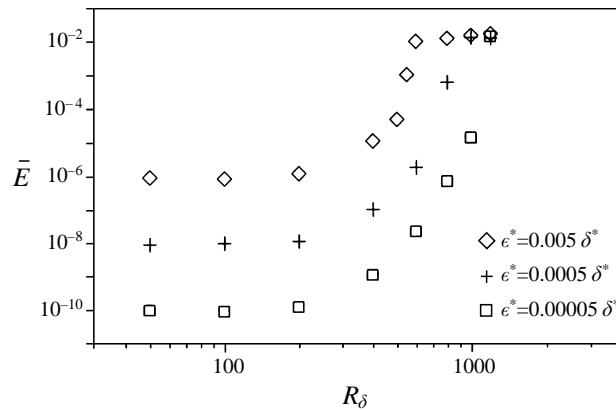


FIGURE 11. Box-averaged specific turbulent kinetic energy  $\bar{E}$  versus  $R_\delta$ .

#### 4. Averaged flow characteristics

In this Section the averaged characteristics of the flow field in the disturbed laminar and intermittently turbulent regimes are presented. Comparisons with experimental results, when possible, will be presented in order to provide further validation of the numerical approach. The procedure employed to obtain averaged values has been defined previously (equation (9)). When necessary to increase the statistical sample, the parity under the transformation  $\varphi \rightarrow \varphi + \pi$  is also employed. From table 1 where the parameters of all the runs are reported, it can be appreciated that for  $R_\delta$  larger



than 400 the statistical sample ranges from a minimum of 6144 to a maximum of 53 248 items.

The averaged profiles of the streamwise velocity component at different phases during the cycle, shown in figures 12 and 13 for  $R_\delta$  equal to 400 and 1000 respectively, indicate that in both the disturbed laminar ( $R_\delta = 400$ ) and intermittently turbulent ( $R_\delta = 1000$ ) regimes, at the beginning of the accelerating part of the cycle, the phase of velocity variations near the wall advances slightly compared with that far from the wall. However, the phase difference in the intermittently turbulent case is much smaller than in the disturbed laminar flow which exhibits velocity profiles very similar to those of the Stokes solution. In figure 13 the experimental results by Akhavan *et al.* (1991*a*) for  $R_\delta = 1080$  are also shown. It can be immediately appreciated that a qualitative agreement between numerical and experimental results is found on the temporal development of velocity profiles, while quantitative discrepancies are present. Such discrepancies can be partly ascribed to the different value of the Reynolds number and partly to the fact that the experiments by Akhavan *et al.* (1991*a*) were conducted in a different geometry which consisted of a circular pipe of radius  $10.6\delta^*$ . Indeed, it is evident from the velocity profiles obtained numerically and shown in figure 13 that in the decelerating phases of the flow the boundary layer thickness attains quite large values with respect to the radius of the duct. For this reason, far from the wall, Akhavan *et al.* (1991*b*) found values of the ratio between the actual velocity and  $U_o^*$  larger than one.

Comparing figures 12 and 13, it is clearly apparent that the thickness of the boundary layer increases in the intermittently turbulent regime and slightly lower velocity values are found near the wall. This tendency towards uniformity of the velocity distributions in the intermittently turbulent regime is caused by the violent turbulent mixing, transferring momentum of high-speed fluid towards the wall and momentum of low-speed fluid far from the wall. Such a tendency is confirmed by the phase dependence of the streamwise component of velocity at different heights from the wall shown in figure 14 for a value of the Reynolds number close to that investigated by Hino *et al.* (1983) together with their measurements. In accordance with the experimental results, it can be observed that the velocity variations near the wall are rather flat for long periods and then are characterized by a rapid change. Moreover, in accordance with Hino *et al.*'s (1983) observations, the present simulations also show small humps towards the end of the decelerating phases in the near-wall region, which are more pronounced in the vicinity of the wall. These humps are produced by the strong increase of turbulence activity which takes place during the decelerating phases in the near-wall region, as can be seen from figure 15 where turbulence intensities are plotted at different phases in the cycle. In figure 15 the experimental measurements of  $\langle u'_1 u'_1 \rangle$  and  $\langle u'_2 u'_2 \rangle$  by Akhavan *et al.* (1991*a*) are also shown. It can be immediately appreciated that while the temporal evolution of turbulent intensities is qualitatively well predicted, quantitative differences are found. As previously discussed, such discrepancies can be ascribed partly to the difference in Reynolds number and partly to the influence of the different geometry of Akhavan *et al.*'s (1991*a*) experiments. It is worth pointing out that turbulent intensities measured by Akhavan *et al.* (1991) do not vanish at the axis of the pipe, thus showing that  $\delta^*$  cannot be considered much smaller than the radius of the duct. The temporal development of the turbulent intensities shows that the term  $\langle u'_1 u'_1 \rangle^{1/2}$  turns out to be always larger than  $\langle u'_2 u'_2 \rangle^{1/2}$  and  $\langle u'_3 u'_3 \rangle^{1/2}$  and it is characterized by a different dynamics. Indeed  $\langle u'_1 u'_1 \rangle^{1/2}$  reaches its maximum intensity

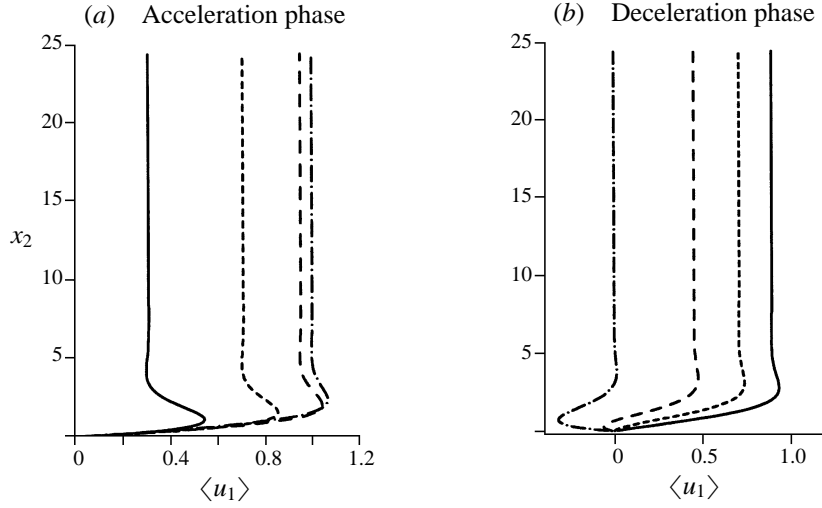


FIGURE 12. Ensemble-averaged velocity profiles (streamwise component) for  $R_\delta = 400$ ,  $\epsilon = 0.005$  (average over three periods). (a) Accelerating phase: —,  $\varphi = \frac{3}{5}\pi$ ; ---,  $\varphi = \frac{3}{4}\pi$ ; - · - ·,  $\varphi = \frac{9}{10}\pi$ ; - · - · - ·,  $\varphi = \pi$ . (b) Decelerating phase: —,  $\varphi = \frac{23}{20}\pi$ ; ---,  $\varphi = \frac{3}{4}\pi$ ; - · - ·,  $\varphi = \frac{27}{20}\pi$ ; - · - · - ·,  $\varphi = \frac{3}{2}\pi$ .

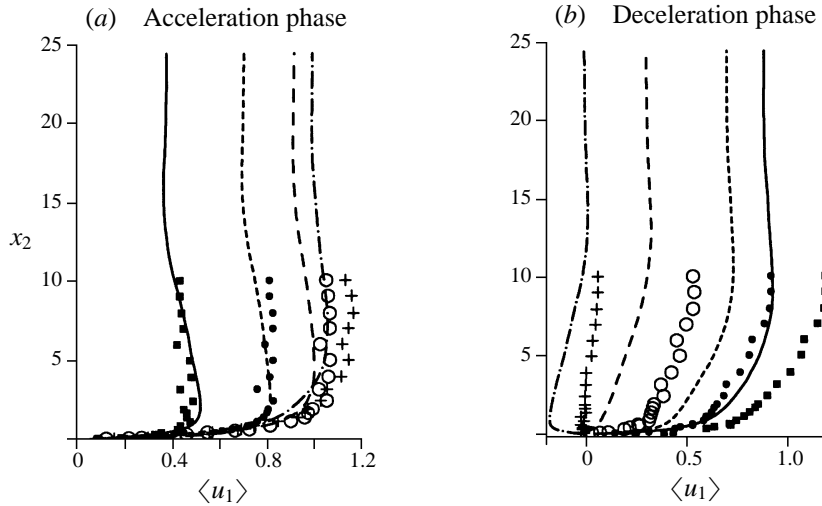


FIGURE 13. Ensemble-averaged velocity profiles (streamwise component) at different phases in the cycle.  $R_\delta = 1000$  (average over six periods). Together with Akhavan *et al.* (1991a) experimental results obtained for  $R_\delta = 1080$  (dots). (a) Acceleration phase: —, ■,  $\varphi = \frac{5}{8}\pi$ ; ---, ●,  $\varphi = \frac{6}{8}\pi$ ; - · - ·, ○,  $\varphi = \frac{7}{8}\pi$ ; - · - · - ·, +,  $\varphi = \pi$ . (b) Deceleration phase: —, ■,  $\varphi = \frac{9}{8}\pi$ ; ---, ●,  $\varphi = \frac{10}{8}\pi$ ; - · - ·, ○,  $\varphi = \frac{11}{8}\pi$ ; - · - · - ·, +,  $\varphi = \frac{12}{8}\pi$ .

at the end the accelerating phase while  $\langle u'_2 u'_2 \rangle^{1/2}$  and  $\langle u'_3 u'_3 \rangle^{1/2}$  attain the largest values during the decelerating phase when turbulent fluctuations are observed to be more intense.

In order to get a deeper insight in the temporal development of turbulence, it is worth considering the equation for the turbulent kinetic energy (Hinze 1959) which

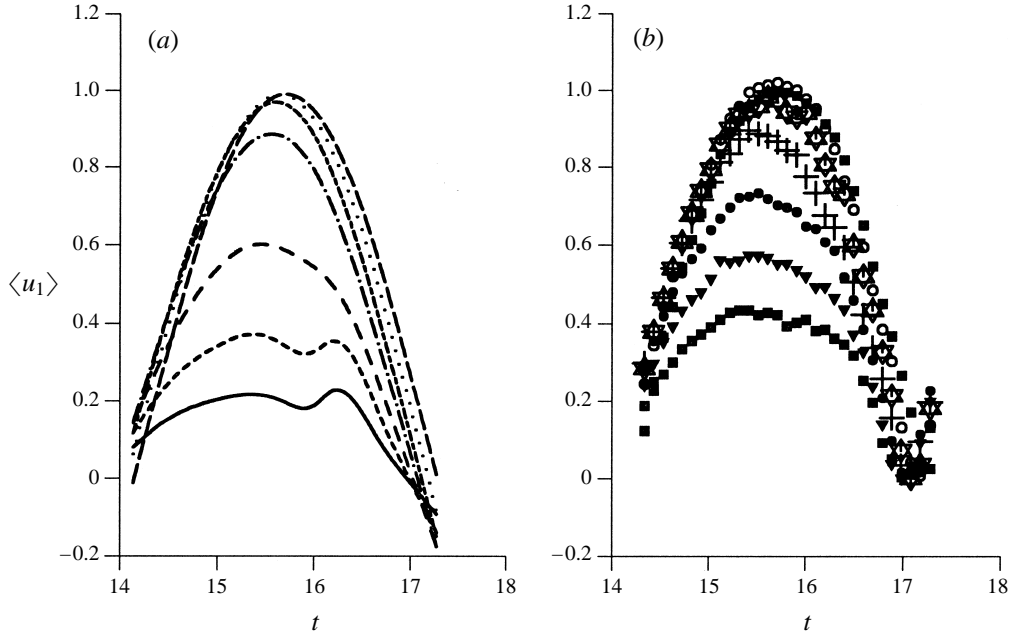


FIGURE 14. Temporal development of the ensemble-averaged streamwise velocity component at various distances from the wall for  $R_\delta = 800$  (a) together with Hino *et al.* (1983) results obtained for  $R_\delta = 876$  (b) —, ■,  $y = 0.128\delta^*$ ; - - - , ▼,  $y = 0.256\delta^*$ ; - - - , ●,  $y = 0.512\delta^*$ ; - · - · - , +,  $y = 1.28\delta^*$ ; - - - - - , ★,  $y = 2.56\delta^*$ ; ·········, ■,  $y = 5.12\delta^*$ ; — — — — — , o,  $y = 12.8\delta^*$ .

in non-dimensional form reads

$$\begin{aligned} \frac{\partial e}{\partial t} = & \underbrace{-\frac{R_\delta}{2}\langle u_j \rangle \frac{\partial e}{\partial x_j}}_{\text{I}} - \underbrace{\frac{R_\delta}{2} \frac{\partial}{\partial x_j} \langle u_j p' \rangle}_{\text{II}} - \underbrace{\frac{R_\delta}{2} \frac{\partial}{\partial x_j} \left( \frac{1}{2} \langle u_i' u_i' u_j' \rangle \right)}_{\text{III}} + \underbrace{\frac{1}{4} \frac{\partial}{\partial x_j \partial x_j} \langle u_i' u_i' \rangle}_{\text{IV}} \\ & - \underbrace{\frac{R_\delta}{2} \langle u_i' u_j' \rangle \frac{1}{2} \left( \frac{\partial \langle u_i \rangle}{\partial x_j} + \frac{\partial \langle u_j \rangle}{\partial x_i} \right)}_{\text{V}} - \underbrace{\frac{1}{2} \left\langle \frac{\partial u_i'}{\partial x_j} \frac{\partial u_i'}{\partial x_j} \right\rangle}_{\text{VI}}, \end{aligned} \quad (14)$$

where the turbulent kinetic energy in non dimensional form turns out to be

$$e = \frac{1}{2} \langle u_i' u_i' \rangle.$$

Differently from the Blasius boundary layer case where all terms appearing in equation (14) show the same order of magnitude, in the present case term I vanishes and term II remains negligible throughout the whole cycle. In figure 16 the vertical distribution of the largest terms appearing in (14) are shown at different phases in the cycle. It can be observed that term V (figure 16 a), describing the production of turbulent kinetic energy, grows during the accelerating phases and at the beginning of the decelerating phases and attains maximum values near the wall at a distance of approximately  $0.5\delta^*$  at a phase  $\varphi$  slightly larger than  $\pi$ . Similarly term VI, which will be referred to as the dissipation term, grows during the accelerating and the first part of the decelerating phases and its reaches maximum value for  $\varphi \approx 23/20\pi$  at a distance of approximately  $0.2\delta^*$  from the wall (figure 16 b). The term describing turbulent convection of kinetic energy (term III) attains its maximum amplitude at the end of the accelerating part of the cycle at the wall, shows a second maximum for a value of  $x_2$  equal to about  $0.5\delta^*$

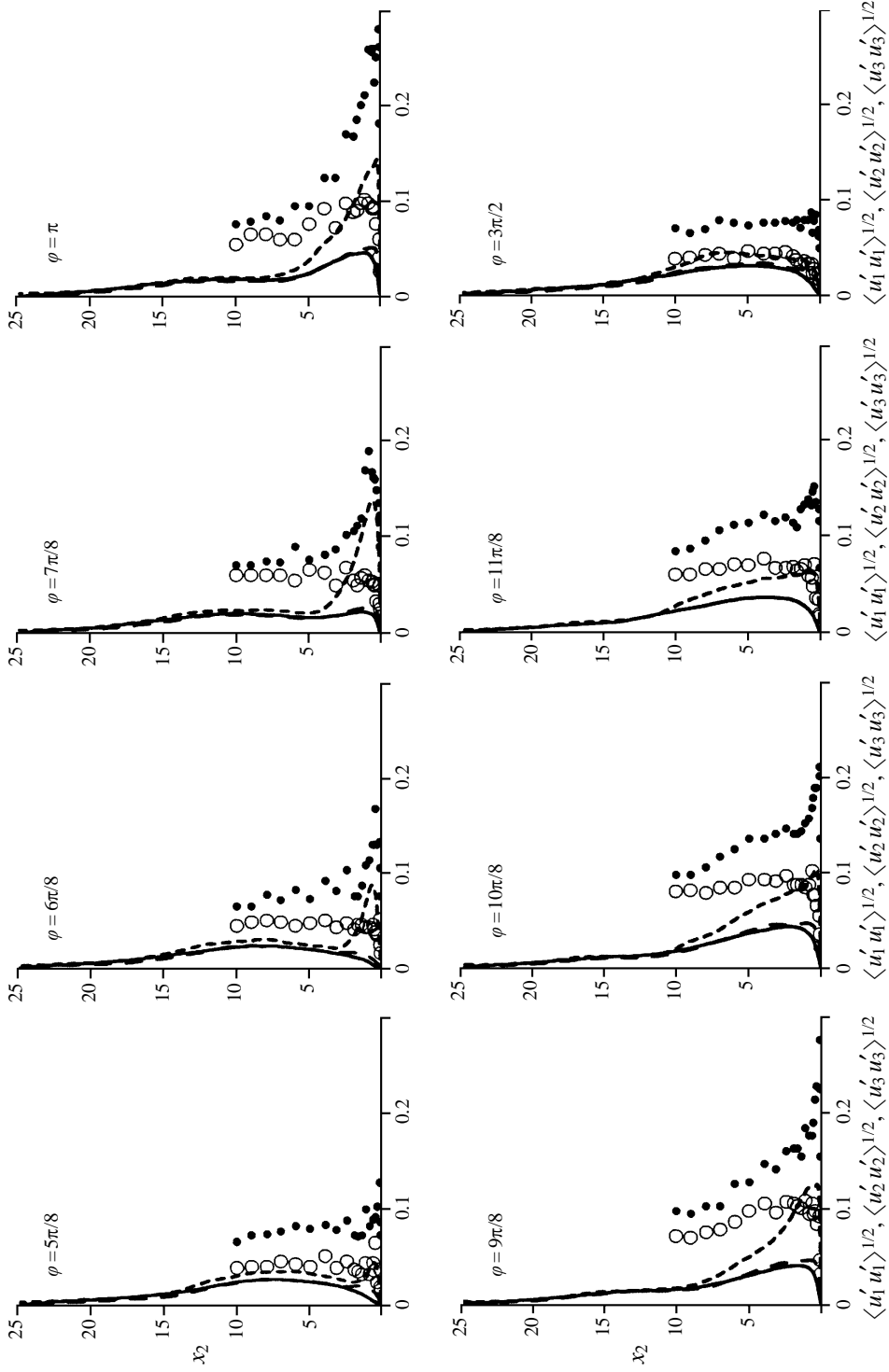


FIGURE 15. Turbulence intensities at different phases in the cycle for  $R_\delta = 1000$  (average over 12 flow fields): - - -,  $\langle u_1' u_1' \rangle^{1/2}$ ; ---,  $\langle u_2' u_2' \rangle^{1/2}$ ; ···,  $\langle u_3' u_3' \rangle^{1/2}$ . Dots: Akhavan *et al.* (1991 a) results obtained for  $R_\delta = 1080$  (•,  $\langle u_1' u_1' \rangle^{1/2}$ ; ◦,  $\langle u_2' u_2' \rangle^{1/2}$ ).

and slowly vanishes in the cross-stream direction (figure 16 *c*). Finally, the influence of the diffusive term (IV) is mainly restricted to the near-wall region and its growth is limited to the early stages of decelerating phases.

From the temporal development of the terms of equation (14) integrated in the vertical direction (see figure 17) it can be immediately appreciated that the terms describing turbulent convection and diffusion of turbulent kinetic energy are significantly smaller than the production and dissipation terms. Moreover, it can be noticed that an order of magnitude balance is attained at each instant between the vertically averaged values of production and dissipation terms. However, inspection of figures 16 (*a*) and 16 (*b*) shows that such a balance is not attained locally. The overall picture emerging from the analysis of the temporal and spatial development of the terms of equation (14) is thus the following. The accelerating phase of the flow is characterized by a rapid production of turbulent kinetic energy which takes place in a wall region of order  $2\delta^*$ . Turbulence in this phase is not in equilibrium since the production term is significantly larger than the dissipation. Hence turbulent energy grows; moreover, it diffuses because of term IV. At later times, because of diffusion the maximum of turbulent kinetic energy moves far from the wall and tends to decrease while  $e$  spreads. In the early part of the decelerating phase the production remains approximately constant while dissipation grows in the region near the wall. In this part of the cycle turbulence appears to be in a situation of quasi-equilibrium. Finally, in the last part of the decelerating phase all the quantities are found to decay and both production and dissipation cover a larger spatial region. The present results are indirectly supported by experimental observations (Hino *et al.* 1973; Akhavan *et al.* 1991 *a*) which show high turbulence fluctuations during the first part of decelerating phases. Moreover, in this phase, due to the effect of term II and of turbulent convection, turbulence tends to become more isotropic and the velocity fluctuations become progressively three-dimensional. This trend is also supported by the output of the 'numerical probe' shown in figure 6.

The results described above show that the dynamics of turbulence is highly time-dependent and quasi-equilibrium conditions are reached only during a restricted part of the decelerating phase.

The high unsteadiness of the flow and of turbulence structure affects both the average velocity and the shear stresses shown in figure 18 together with the experimental results by Akhavan *et al.* (1991 *a*). It can be appreciated that the viscous component appears to be significant only in a layer of order  $\delta^*$  adjacent to the wall. On the other hand the turbulent contribution is found to grow towards the end of the accelerating part of the cycle and to reach its maximum intensity during the decelerating part at a distance from the wall of approximately  $2\delta^*$  even though it remains significant in a near-wall region of thickness about  $15\delta^*$ . From figure 18, it can be seen that also the temporal development of turbulent shear stress is in agreement with experimental results. Good agreement with existing experimental results is also attained regarding the temporal development of horizontally averaged wall shear stress shown in figure 19 for  $R_\delta = 1000$ . The wall shear stress turns out to be maximum at the end of the accelerating and early decelerating phases and is practically in phase with the outer velocity.

## 5. Conclusions

On the basis of direct simulations of an oscillatory flow close to a flat but imperfect wall, it has been possible to delineate the mechanism of transition from the laminar to the intermittently turbulent regime through the disturbed laminar regime in a Stokes boundary layer. In the disturbed laminar regime it has been shown that the

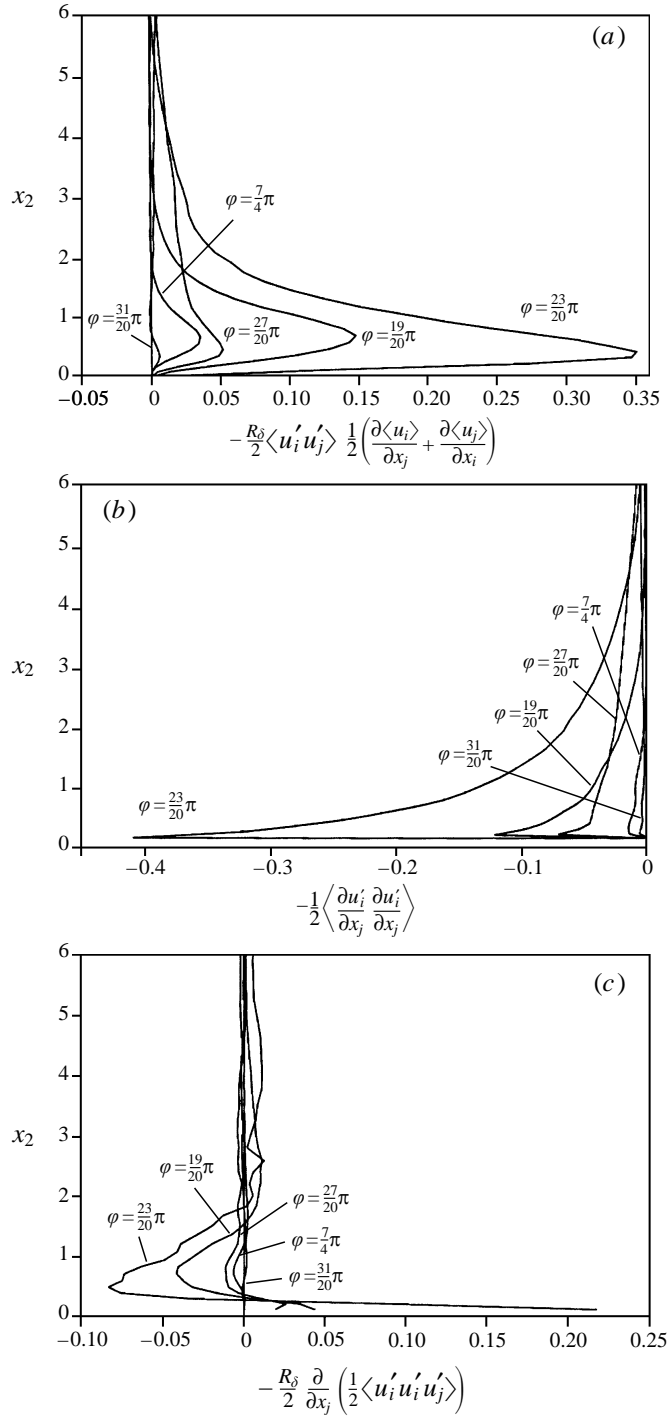


FIGURE 16 (a-c). For caption see facing page.

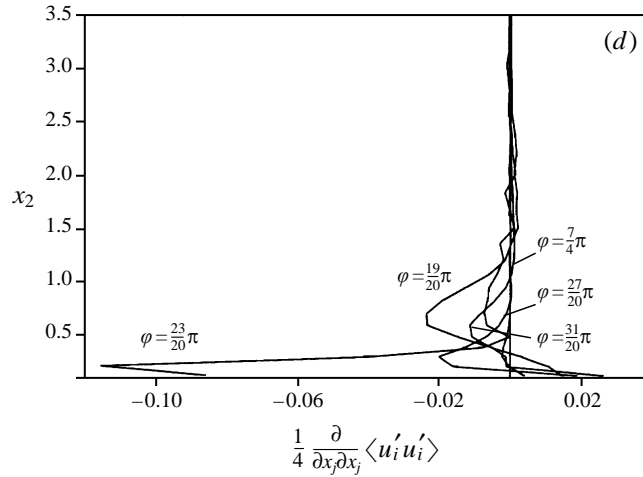


FIGURE 16. Vertical distribution of the different terms appearing in equation (14) at different phases during the cycle;  $R_\delta = 800$  (average over 26 flow fields): (a) production of turbulent kinetic energy (V term in (14)), (b) dissipation of turbulent kinetic energy (VI term in (14)), (c) turbulent convection (III term in (14)), (d) diffusion (IV term in (14)).

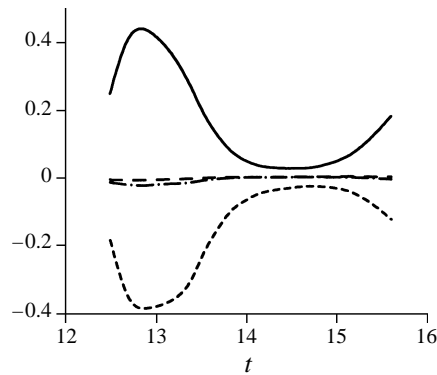


FIGURE 17. Temporal development of vertical integrated value of the terms of equation (14),  $R_\delta = 800$ : —, production (term V); - - - -, dissipation (term VI); - · - · -, turbulent convection (term III); - · - · - · -, diffusion (term IV).

disturbances observed in experiments are induced by imperfections of the experimental apparatus which in turn excite the modes known to be momentarily unstable on the basis of the momentary stability analysis of Blondeaux & Seminara (1979). The flow field in the disturbed laminar regime turns out to be highly two-dimensional and periodic. As  $R_\delta$  exceeds 550 three-dimensional components appear in accordance with the results by Akhavan *et al.* (1991*b*) and the 'intermittently turbulent regime' is observed.

Moreover, the numerical simulations have shown that the value of the time-averaged vertically integrated specific kinetic energy of the disturbances depends both on the Reynolds number and on the amplitude of wall imperfections in the 'disturbed laminar' regime, while in the 'intermittently turbulent' regime  $\bar{E}$  is found to be independent of  $\epsilon$  and to depend only weakly on  $R_\delta$ . The runs for Reynolds numbers in the intermittently turbulent regime have allowed the characteristics of turbulence to be investigated. In particular the analysis of the temporal development of the

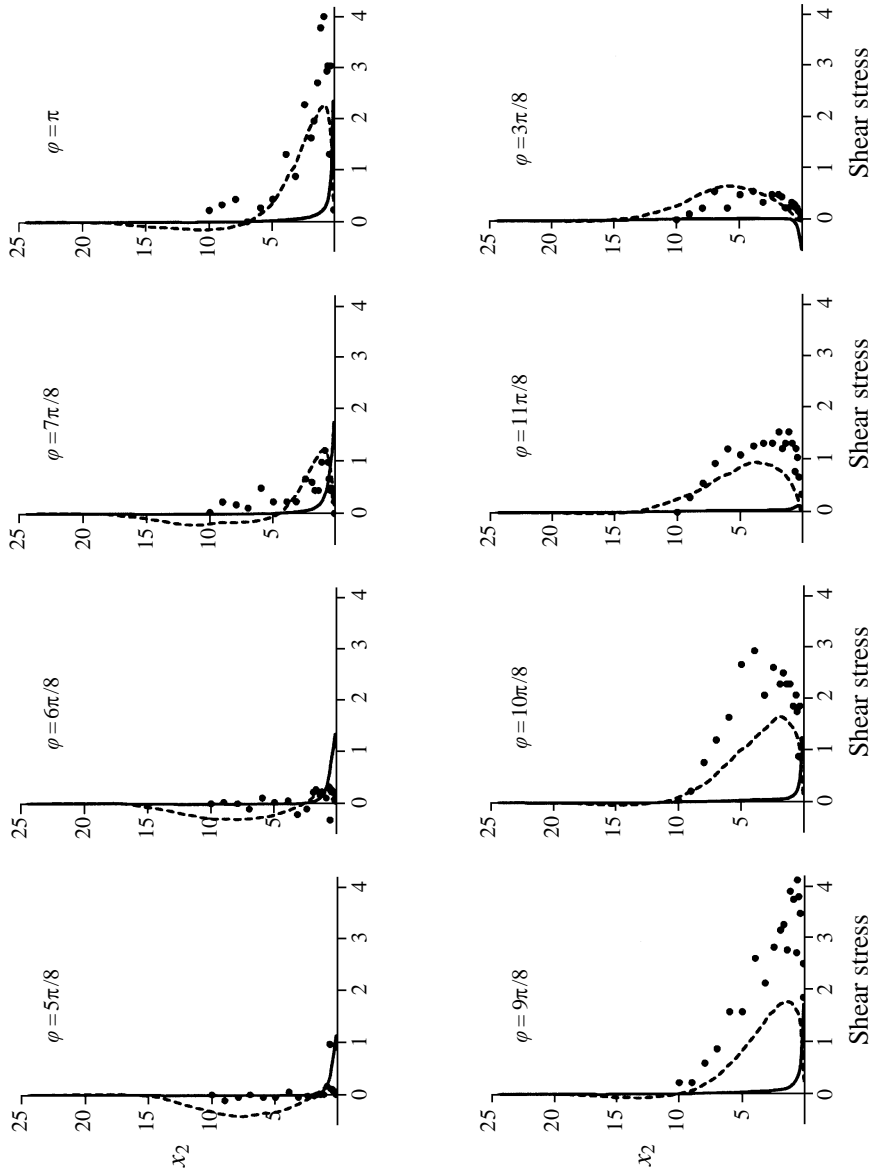


FIGURE 18. Vertical distribution of shear stress at different phases in the cycle ( $Re_s = 800$ ): —, laminar component; - - -, turbulent component; ●, experimental results by Akhavan *et al.* (1991 *a*).



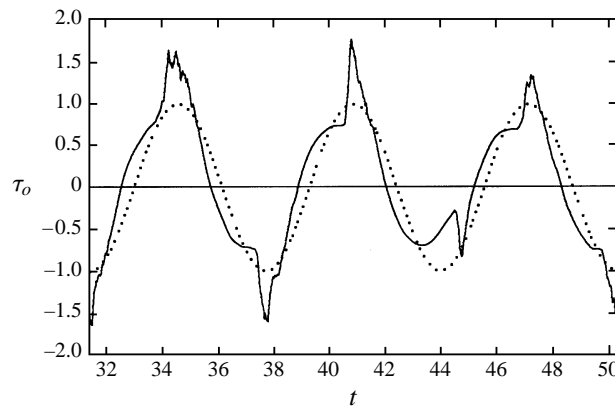


FIGURE 19. Temporal development of the horizontally averaged wall shear stress ( $\tau_o$ ) at  $R_\delta = 1000$  (—) and temporal development of streamwise velocity component far from the wall (.....).

different terms of the turbulent kinetic energy equation has shown that equilibrium conditions are never strictly attained. Indeed while the accelerating part of the cycle is characterized by turbulence production, dissipation starts to be effective during the decelerating phase. Therefore, 'quasi-equilibrium' conditions are observed only during a small part of the decelerating phase.

This research has been partly supported by the Office of Naval Research (O.N.R.) under contract n. N00014-97-1-0790, by the EU under the contract MAS3-CT97-0115 'SEDMOC' in the framework of the Marine Science and Technology Programme (MAST-III) and by the "Ministero dell'Università e della Ricerca Scientifica e Tecnologica" under the contract 'Processi vorticosi, turbolenti, caotici'.

#### REFERENCES

- AKHAVAN, R., KAMM, R. D. & SHAPIRO, A. H. 1991 *a* An investigation of transition to turbulence in bounded oscillatory Stokes flows. Part 1. Experiments. *J. Fluid Mech.* **225**, 395–422.
- AKHAVAN, R., KAMM, R. D. & SHAPIRO, A. H. 1991 *b* An investigation of transition to turbulence in bounded oscillatory Stokes flows. Part 2. Numerical simulations. *J. Fluid Mech.* **225**, 423–444.
- BEAM, R. M. & WARMING, R. F. 1976 An implicit finite-difference algorithm for hyperbolic system in conservation-law form. *J. Comput. Phys.* **22**, 87.
- BLONDEAUX, P. 1990 Sand ripples under sea waves. Part 1. Ripple formation. *J. Fluid Mech.* **218**, 1–17.
- BLONDEAUX, P. & SEMINARA, G. 1979 Transizione incipiente al fondo di un'onda di gravità. *Rendiconti Accad. Naz. Lincei* **67**, 407–417.
- BLONDEAUX, P. & VITTORI, G. 1994 Wall imperfections as a triggering mechanism for Stokes-layer transition. *J. Fluid Mech.* **264**, 107–135.
- COWLEY, S. J. 1987 High frequency Rayleigh instability of Stokes layers. In *Stability of Time Dependent and Spatially Varying Flows* (ed. D. L. Dwayee & M. Y. Hussaini), pp. 261–275. Springer.
- ECKMANN, D. M. & GROTEBERG, J. B. 1991 Experiments on transition to turbulence in oscillatory pipe flow. *J. Fluid Mech.* **222**, 329–350.
- HALL, P. 1978 The linear stability of flat Stokes layers. *Proc. R. Soc. Lond. A* **359**, 151–166.
- HINO, M., KASHIWAYANAGI, M., NAKAYAMA, A. & HARA, T. 1983 Experiments on the turbulence statistics and the structure of a reciprocating oscillatory flow. *J. Fluid Mech.* **131**, 363–400.
- HINO, M., SAWAMOTO, M. & TAKASU, S. 1976 Experiments on transition to turbulence in an oscillatory pipe flow. *J. Fluid Mech.* **75**, 193–207.

- HINZE, J. O. 1959 *Turbulence*. McGraw-Hill.
- JENSEN, B. L., SUMER, B. M. & FREDSE, J. 1989 Turbulent oscillatory boundary layers at high Reynolds numbers. *J. Fluid Mech.* **206**, 265–297.
- KIM, J. & MOIN, P. 1985 Application of a fractional-step method to incompressible Navier–Stokes equations. *J. Comput. Phys.* **59**, 308.
- MONKEWITZ, A. A. 1983 Lineare stabilitätsuntersuchungen an den oszillierenden Grenzschichten von Stokes. PhD thesis 7297, Federal Institute of Technology, Zurich, Switzerland.
- ORLANDI, P. 1989 A numerical method for direct simulation of turbulence in complex geometries. *Annual Research Brief*, 215. Center for Turbulence Research, Stanford University.
- RAI, M. M. & MOIN, P. 1991 Direct simulations of turbulent flow using finite-difference schemes. *J. Comput. Phys.* **96**, 15.
- SARPKAYA, T. 1993 Coherent structures in oscillatory boundary layers. *J. Fluid Mech.* **253**, 105–140.
- SPALART, P. R. & BALDWIN, B. S. 1987 Direct simulation of a turbulent oscillating boundary layer. *6<sup>th</sup> Symp. on Turbulent Shear Flows, Toulouse 7–9 September* (ed. F. Durst, B. Launder, F. Schmidt & J. Whitelaw).
- STOKES, G. G. 1855 On the effects of internal friction of fluids on the motion of pendulums. *Trans. Camb. Phil. Soc.* **9**.
- TROMANS, P. 1976 The stability of oscillatory pipe flow. Abstract of lecture given at Euromech 73: *Oscillatory Flows in Ducts, Aix-en-Provence, April 13–15*.
- VERZICCO, R. & VITTORI, G. 1996 Direct simulation of transition in a Stokes boundary Layer *Phys. Fluids* **8**, 1341–1343.
- VITTORI, G. 1992 Flow field induced by sea waves over brick-pattern ripples. *J. Hydraulic Engng ASCE* **118**, 1241.
- VON KERCZEK, C. & DAVIS, S. H. 1974 Linear stability theory of oscillatory Stokes layers. *J. Fluid Mech.* **62**, 753–773.
- WU, X. 1992 The nonlinear evolution of high-frequency resonant triad waves in an oscillatory Stokes layer at high Reynolds number. *J. Fluid Mech.* **245**, 553–597.
- WU, X., LEE, S. S. & COWLEY, S. J. 1995 On the weakly nonlinear three-dimensional instability of shear layers to pairs of oblique waves: the Stokes layer as a paradigm. *J. Fluid Mech.* **253**, 681–721.